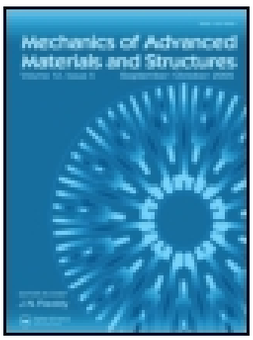

Mechanics of Advanced Materials and Structures

ISSN: 1537-6494 (Print) 1537-6532 (Online) Journal homepage: http://www.tandfonline.com/loi/umcm20

Hyperelastic analysis based on a polygonal finite element method

Amirtham Rajagopal , Markus Kraus & Paul Steinmann

To cite this article: Amirtham Rajagopal , Markus Kraus & Paul Steinmann (2017): Hyperelastic analysis based on a polygonal finite element method, Mechanics of Advanced Materials and Structures, DOI: 10.1080/15376494.2017.1329463

To link to this article: http://dx.doi.org/10.1080/15376494.2017.1329463

Accepted author version posted online: 01 Jun 2017.

Hyperelastic analysis based on a polygonal finite element method

Amirtham Rajagopal*, Markus Kraus†and Paul Steinmann‡

March 18, 2017

Abstract

In this contribution, we present a novel polygonal finite element method applied to hyperelastic analysis. For generating polygonal meshes in a bounded period of time we use the adaptive Delaunay tessellation (ADT) proposed by Constantinu et al [12]. ADT is an unstructured hybrid tessellation of a scattered point set that minimally covers the proximal space around each point. In this work, we have extended the ADT to non-convex domains using concepts from constrained Delaunay triangulation (CDT). The proposed method is thus based on a constrained adaptive Delaunay tessellation (CADT) for the discretization of domains into polygonal regions. We involve the metric coordinate (Malsch) method for obtaining the interpolation over convex and non convex domains. For the numerical integration of the Galerkin weak form we resort to classical Gaussian quadrature based on triangles. Numerical examples of two dimensional hyperelasticity are considered to demonstrate the advantages of the polygonal finite element method.

Keywords: Hyperelasticity, polygonal finite element, adaptive Delaunay tessellation, polygonal interpolant,

*Associate Professor, Department of Civil Engineering, Indian Institute of Technology Hyderabad 502205.

†AUDI AG, Strength and Durability Group, Ingolstadt, Germany 85045

‡Professor and Head, Chair of Applied Mechanics, University of Erlangen, Nuremberg, Germany D91058

1 Introduction

A large strain analysis typically includes both geometric and material non-linearities. For many materials, linear elastic models do not accurately describe the observed material behavior. The most common example of this kind of material is rubber, whose stress-strain relationship can be defined as non-linearly elastic, isotropic, incompressible and generally independent of strain rate. Hyperelasticity provides a means of modeling the stress-strain behavior of such materials. Filled elastomers and biological tissues are also often modeled via the hyperelastic idealization. A hyperelastic material derives the stress-strain relationship from a strain energy density function. Classically the finite element method has been used as a tool for numerical hyperelastic analysis. Advancements in constructions of $n-$gons[1] and interpolants has helped to move beyond the limits of using simple geometrical elements for discretization. The use of $n-$gons provides greater flexibility in dealing with arbitrary geometries. Polygonal finite element discretizations are used in many areas, a few examples include: as interface elements for connecting dissimilar finite element meshes [18], nonlinear constitutive modeling of polycrystalline ferroelectrics [49], two field methods for solving diffusion equations [23], analysis of solid mechanics problems [38] including incompressible materials [13], and for topology optimization [51]. There have been other recent works on developing polygonal finite element interpolants based on scaled boundary elements [10] and virtual nodes [53], obtaining higher order p adaptive and C^k generalized approximations for polygonal clouds [3]. The recent focus has also been on generating conformal polygonal discretizations [25]. Some recent works are also concerned with developing numerical integration schemes for polygonal finite element methods either based on conformal mapping [34] [35] or generalizing Gaussian quadrature rules for polygons [24], [33]. Sukumar et al [46] established the connections between the virtual element method (VEM) and the hourglass control techniques and showed quantitative comparisons of the consistency and stabilization matrices in the VEM to those in the hourglass control method. Heng et al [9] have given an approach towards the challenging task of modeling nonlinear elastic materials with standard finite elements and have proposed an alternative approach to model finite elasticity problems in two dimensions by using polygonal discretization. Gianmarco et al [32] worked on the new perspec-

[1] A $n-$ sided polygon is termed as an $n-$gon

tives on polygonal and polyhedral finite element methods. Floater et al [31] have discussed on gradient bounds for Wachspress coordinates on polytopes. An approach regarding polygonal finite elements approximation for mixed formulations was given by Cameron et al. [52] for incompressible fluid flow. It has been demonstrated that a certain class of approximants can be devoid of spurious modes and locking. Cameron et al. [50] proposed a polygonal finite element procedure for topology optimization. In another recent work [52] integration errors in polygonal finite element methods and its relevance for the patch test have been discussed. Arun et al. [2] proposed the Virtual Element Method (VEM) for the numerical solution of boundary value problems on arbitrary polyhedral meshes and also presented several numerical studies in order to verify convergence of the VEM and evaluate its performance for various types of meshes. Khoei et al. [4] presented a polygonal-FEM technique for modeling of arbitrary interfaces in large deformations and applied it to capture discontinuous deformations in non-conformal elements, which are cut by the interface in a uniform regular mesh. Biabanaki et al. [5] presented a polygonal finite element method for large deformation frictionless dynamic contact-impact problems with non-conformal meshes. Sukumar et al. [44] presented the development of quadratic serendipity shape functions on planar convex and nonconvex polygons and maximized the objective functional subject to the constraints for quadratic completeness. A numerical algorithm based on group theory and numerical optimization was presented by Mousavi et al. [33] to compute efficient quadrature rules for integration of the bivariate polynomials over arbitrary polygons. The algorithm was used for the construction of symmetric and non-symmetric quadrature rules over convex and concave polygons. Nguyen et al. [37] provided an approach towards free and forced vibration analysis using the n-sided polygonal cell-based smoothed finite element method. They further extended the nCS-FEM to the free and forced vibration analyses of two dimensional (2D) dynamic problems. Hornmann et al [21] introduced a new generalization of barycentric coordinates that stems from the maximum entropy principles. David et al [14] presented a mixed-element mesh generator based on the modified octree approach that has been adapted to generate polyhedral Delaunay meshes. Yijiang et al. [60] presented an explicit expression of two-dimensional element compliance matrix on the complementary energy principle with concave polygonal meshes. Dai et al [13] proposed a smoothed finite element method (SFEM) using quadrilateral elements, whereby the method produces very accurate stresses and desirable convergence rate comparable to the FEM.

Kraus and Steinmann [22] presented finite element formulations for 3D convex polyhedra in nonlinear continuum mechanics. An n- sided polygonal edge - based smoothed finite element method (nES-FEM) for solid mechanics problems is discussed in [37]. Somnath et al [20] developed a Voronoi cell finite element method to solve small deformation elastic-plastic problems for arbitrary heterogeneous materials and conducted studies to understand the effect of size, shape and distribution of second phases on the averaged and true local responses of representative material elements. Zhang et al. [62] developed a parametric variational principle based polygonal finite element method (PFEM) and Voronoi cell finite element method (VCFEM) for the numerical simulation of the elastic–plastic mechanical behavior of heterogeneous materials under small deformation and also gave the shape functions for the polygonal element. Sundararajan et al. [36] studied the convergence and accuracy of displacement based finite element formulations over arbitrary polygons. Laplace interpolants, strain smoothing and scaled boundary polygon formulations were considered for the analysis. Andrew et al. [1] studied error estimates for generalized barycentric interpolation. An efficient numerical scheme for the biharmonic equation by weak Galerkin finite element methods on polygonal or polyhedral meshes has been proposed in [11]. Higher order BEM-based FEM on polygonal meshes have been studied recently (see [39] and [40]).

In this work we present a Galerkin method based on adaptive Delaunay tessellation (ADT) over non-convex geometries for solving two-dimensional geometrically nonlinear hyperelasticity problems. Various polygonal interpolants available in the literature amongst others include Laplace, Wachpress [55], Warren [57], and Floaters mean value interpolants [19]. In the present work, we make use of the metric coordinate method or rather Malsch interpolant [30] for the interpolation over non-convex polygonal domains. Thereby we use a mapping of a star shaped polygonal physical element to a canonical element.

In section 2 we present the governing equations and weak form of hyperelastic analysis. An overview of the novel ADT hybrid polygonal meshing technique for scattered point distribution as proposed in Constantiniu et al. [12] is presented in section 3. In section 4 the methodology for computing Malsch interpolants [30] are discussed. In the last section we present numerical examples in two dimensions to test the polygonal finite element method for hyperelastic materials.

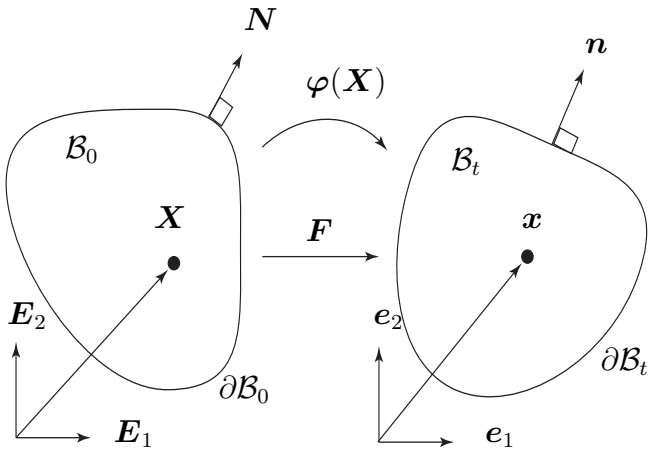

Figure 1: Elastostatic boundary value problem.

2 Governing equations and weak form

To state the variational principle in a geometrically nonlinear setting we refer all quantities arising in the continuum mechanical description to the material configuration $\mathcal{B}_0 \subset \Re^3$ with boundary $\partial\mathcal{B}_0$ and outward units normal vector $\boldsymbol{N}$. In defining the motion of $\mathcal{B}_0$ a typical continuum particle occupies a succession of points which for a fixed material point $\boldsymbol{X}$ forms the spatial path for this continuum particle (see Figure 1). The position vectors of particles in $\mathcal{B}_0$ are given by $\boldsymbol{X}$, and the nonlinear deformation map

$$\boldsymbol{\varphi} : \mathcal{B}_0 \to \mathcal{B}_t \tag{1a}$$

$$\boldsymbol{X} \mapsto \boldsymbol{\varphi}\left(\boldsymbol{X}\right) = \boldsymbol{x} \tag{1b}$$

is such that it maps particles $\boldsymbol{X}$ of the material configuration to particles $\boldsymbol{x}$ in the spatial configuration $\mathcal{B}_t$. As usual $\boldsymbol{\varphi}$ is assumed to be sufficiently smooth (C^1 continuous) so that we define the deformation gradient.

$$\boldsymbol{F} := \nabla_X \boldsymbol{\varphi}, \;\; F_{iA} := \frac{\partial \varphi_i}{\partial X_A}, \tag{2}$$

where we use small and capital indices which refer either to the spatial or the material configuration, respectively. It is observed that $\boldsymbol{F}$ is a second order two point tensor that does not exhibit any symmetries. The Jacobian determinant is denoted by $J := \det\boldsymbol{F} = dv/dV > 0$, with dV and dv being

the infinitesimal volume elements in the material and spatial configuration, respectively.

2.1 Energy minimization and balance relations

We consider a hyperelastic continuum for which the potential energy Π is a functional of the deformation, $\boldsymbol{\varphi}$, whereas the stored energy density W_0 depends on $\boldsymbol{F}$ and $\boldsymbol{X}$, so that the functional is written as

$$\Pi\left(\boldsymbol{\varphi}\right) = \int\limits_{\mathcal{B}_0} W_0\left(\boldsymbol{F}, \boldsymbol{X}\right) dV + \Pi^{ext}(\boldsymbol{\varphi}). \tag{3}$$

If we assume the material to be hyperelastic, stresses can be defined as the derivatives of W_0 with respect to their energetically conjugate deformation variables. The Piola- type macro-stress $\boldsymbol{P}$,

$$\boldsymbol{P} := \partial_F W_0. \tag{4}$$

For arbitrary variations $\delta\boldsymbol{\varphi}$, the energy minimization takes the form

$$\delta\Pi = \delta\Pi^{\text{int}} + \delta\Pi^{\text{ext}} = 0, \tag{5}$$

where

$$\delta\Pi^{\text{ext}} := -\int\limits_{\mathcal{B}_0} \boldsymbol{b}_0 \cdot \delta\boldsymbol{\varphi} dV - \int\limits_{\partial\mathcal{B}_0} \delta\boldsymbol{\varphi} \cdot \boldsymbol{t}_0^p dA. \tag{6}$$

In the above equation, $\boldsymbol{b}_0$ is the body force density acting on the material domain $\mathcal{B}_0$ and $\boldsymbol{t}_0^p$ is the nominal surface traction which acts on the Neumann surface in the material configuration $\partial\mathcal{B}_0^t$. By application of the Gauss theorem, we derive the equilibrium equations and Neumann- type boundary conditions. Integrating by parts, variation of the internal energy term becomes

$$\delta\Pi^{int} = -\int\limits_{\mathcal{B}_0} \delta\boldsymbol{\varphi} \cdot \text{Div}\boldsymbol{P} dV + \int\limits_{\partial\mathcal{B}_0{}^t} \delta\boldsymbol{\varphi} \cdot \boldsymbol{P} \cdot \boldsymbol{N}\, dA$$

Thus the variation of the total potential energy is given by

$$\begin{aligned}\delta\Pi = \quad & -\int\limits_{\mathcal{B}_0} \delta\boldsymbol{\varphi} \cdot \text{Div}\boldsymbol{P} dV + \int\limits_{\partial\mathcal{B}_0^t} \delta\boldsymbol{\varphi} \cdot \boldsymbol{P} \cdot \boldsymbol{N}\, dA \\ & -\int\limits_{\mathcal{B}_0^t} \boldsymbol{b}_0 \cdot \delta\boldsymbol{\varphi} dV - \int\limits_{\partial\mathcal{B}_0^t} \delta\boldsymbol{\varphi} \cdot \boldsymbol{t}_0^p dA = 0,\end{aligned}$$

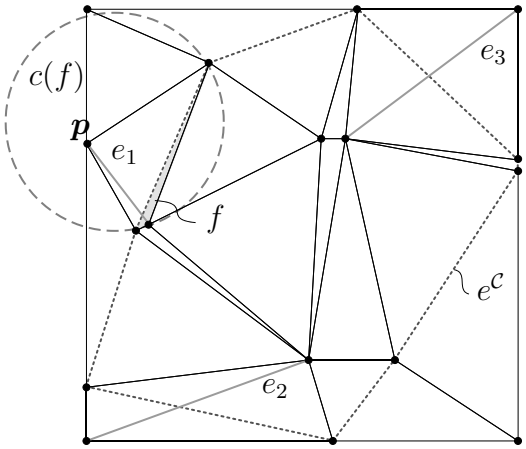

Figure 2: Delaunay and constrained Delaunay tessellation: the edges e_1, e_2 and e_3 of the initial DT($\mathcal{N}$) are not strongly Delaunay, as with the enabled constraining edges $e^{\mathcal{C}}$ (dotted lines) an edge flipping is triggered. The triangle f is then also constraint Delaunay although point $\boldsymbol{p}$ is inside the circumcircle $c(f)$ but not Delaunay visible.

Following the common steps we can write the equilibrium equations as

$$\operatorname{Div} \boldsymbol{P} = -\boldsymbol{b}_0 \quad \text{in } \mathcal{B}_0 \tag{7}$$

with

$$\boldsymbol{P} \cdot \boldsymbol{N} = \boldsymbol{t}_0^p \quad \text{on } \partial\mathcal{B}_0^t \tag{8}$$

FIGURE 3 FIGURE 4

2.2 Constitutive assumption for stored energy density

A hyperelastic constitutive theory is chosen. Using this constitutive assumption, the stress measures are derived. For the stored energy density W_0, we assume the following hyperelastic Neo- Hookean constitutive function

$$W_0(\boldsymbol{F}) = \frac{1}{2}\lambda \ln^2 J + \frac{1}{2}\mu \left[\boldsymbol{F} : \boldsymbol{F} - n^{\dim} - 2\ln J\right] \tag{9}$$

Herein, the material parameters λ and μ are the Lamé constants from classical elasticity, n^{dim} denotes the number of dimension in space. With this

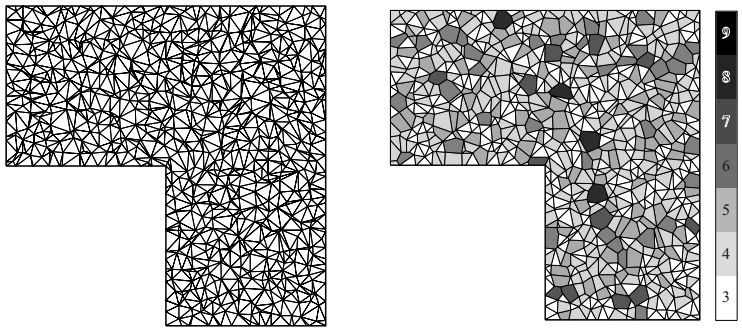

(a) (b)

Figure 3: CDT and associated CADT meshes on non-convex L-shaped domain (a) CDT with 1537 triangular elements, (b) CADT with 863 polygonal elements

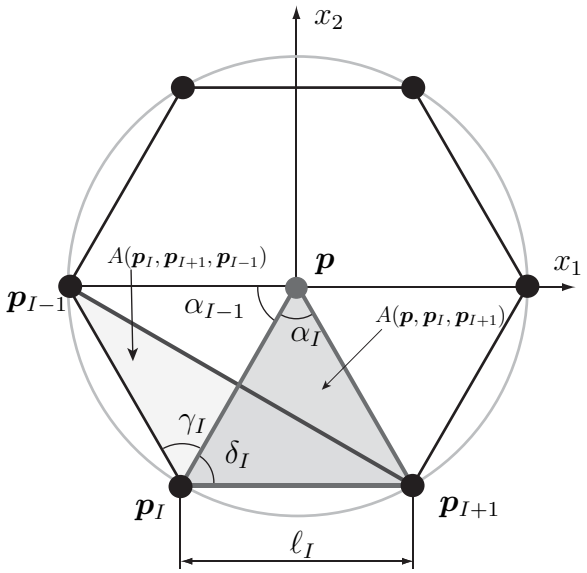

Figure 4: Geometric measures used for polygonal interpolation : signed triangle areas A, section angles α_I, internal polygonal angles γ_I and δ_I for node I.

constitutive assumption the Piola stress takes the form

$$\boldsymbol{P} = \partial_F W_0 = [\lambda \ln J - \mu]\, \boldsymbol{F}^{-T} + \mu \boldsymbol{F}. \tag{10}$$

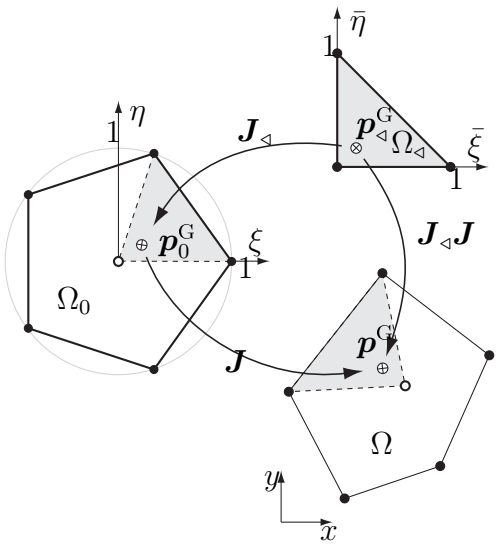

Figure 5: Numerical integration based on partition of the canonical domain Ω_0 or the physical domain Ω and mapping of quadrature points from a generic triangular domain $\Omega_\triangleleft$.

3 Constrained adaptive Delaunay tessellation

We consider a set of nodes $\mathcal{N} = \{\boldsymbol{p}_1, \boldsymbol{p}_2, \ldots \boldsymbol{p}_M\}$ with $\boldsymbol{p}_I \in \mathbb{R}^2$. The first order Voronoi diagram $\mathcal{V}(\mathcal{N})$ of the set $\mathcal{N}$ is a subdivision of the Euclidian space $\mathbb{R}^2$ into convex regions

$$V(\boldsymbol{p}_I) = \left\{\boldsymbol{p} \in \mathbb{R}^2 : ||\boldsymbol{p} - \boldsymbol{p}_I|| < ||\boldsymbol{p} - \boldsymbol{p}_J|| \;\forall\; J \neq I\right\}$$

called Voronoi cells, where $\mathcal{V}(\mathcal{N}) = \cup V(\boldsymbol{p}_I)$ [49, 51, 53–56]. The above definition states that any point $\boldsymbol{p}$ in the Voronoi cell $V(\boldsymbol{p}_I)$ is closer to node $\boldsymbol{p}_I$ than to any other node $\boldsymbol{p}_J$. We can define the Delaunay tessellation $\mathrm{DT}(\mathcal{N})$ such that no other point of $\mathcal{N}$ is inside the circumcircle of the considered triangle in $\mathrm{DT}(\mathcal{N})$. In general, the Delaunay tessellation in a k-dimensional Euclidian space consists of k-simplices (in 2D: triangles) constructed as the convex hull of $k+1$ affinely independent points. The Delaunay tessellation is dual to the Voronoi diagram, maximizes the minimum angle of all the angles of the triangles in the tessellation and tends to avoid skinny triangles.
Factors such as non-uniqueness and geometric qualities of the Delaunay tessellation are of interest. The non-uniqueness is of concern especially in the

case of degenerated subsets of the point set $\mathcal{N}$. Problems arise when three points of a potential triangle are collinear or four or more points are co-circular. This typically happens in the case when a set of planar points is a subset of a rectangular array of points. In such cases the length of a Voronoi edge is zero, hence the corresponding Delaunay edges are missing in the dual graph and non-simplicial polygons are formed. These can be arbitrarily triangulated because their topology remains undefined by merely stating an empty circumcircle (Delaunay) criterion. The geometric qualities of such elements strongly influence the condition number of the stiffness matrix and the numerical accuracy of the approximation scheme [41]. A simple solution for the non-uniqueness is by merging some of these co-circular points like in the extended Delaunay tessellation (EDT) [7]. Recently Constantiniu et al. [12] have proposed the adaptive Delaunay tessellation (ADT) of degenerated point sets. The method is an unstructured hybrid tessellation of a scattered point set that minimally covers the proximal space around each point. The mesh is automatically obtained in a bounded period of time by using geometric properties of an initial Delaunay tessellation. Rigorous proofs for the geometric properties of the ADT have been given by Bobach et al. [6], which include the uniqueness of the ADT, the connectedness of the ADT, and the coverage of the Voronoi tiles by adjacent ADT tiles. These properties indicate that the method is robust for application to solve elasticity problems. In the present work, the ADT proposed in [12] is extended to include also non-convex domains.

For the considered set $\mathcal{N}$ we denote its convex hull as $\mathrm{CH}(\mathcal{N})$, its border as $\partial\mathrm{CH}(\mathcal{N})$ and its associated Delaunay tessellation $\mathrm{DT}(\mathcal{N}) := (\mathcal{E}_{\mathrm{DT}}, \mathcal{F}_{\mathrm{DT}})$ composed by the active edges-to-node tuple $e \subset \mathcal{E}_{\mathrm{DT}} \in \mathbb{N}^2$ and assembled triangles $f \subset \mathcal{F}_{\mathrm{DT}} \in \mathbb{N}^3$. Any triangle f having an interior angle greater than or equal to $\frac{\pi}{2}$ is obtuse. The longest edge of an obtuse triangle $f^>$ opposite to the obtuse angle is denoted as $e_f^>$. For a triangle $f \in \mathcal{F}_{\mathrm{DT}}$ we denote its circumcenter of the circumcircle $c(f)$ by $\boldsymbol{p}_c(f)$. One can state that a triangle f is deemed to be obtuse if it does not contain $\boldsymbol{p}_c(f)$ in its interior and $\boldsymbol{p}_c(f)$ lies on the opposite side of $e_f^>$, respectively (compare with Thales circle). With the set $\mathcal{E}^> = \{e_f^> \mid f \in \mathcal{F}_{\mathrm{DT}} \wedge e_f^> \notin \partial\mathrm{CH}(\mathcal{N})\}$ of all obtuse edges, the tessellation of the domain $\mathrm{CH}(\mathcal{N})$ represented by $(\mathcal{F}_{\mathrm{ADT}}, \mathcal{E}_{\mathrm{DT}} \setminus \mathcal{E}^>)$, where $\mathcal{F}_{\mathrm{ADT}}$ is then the set of polygons generated by merging triangles with common edge in $\mathcal{E}^>$ is the adaptive Delaunay tessellation $\mathrm{ADT}(\mathcal{N})$. The $\mathrm{ADT}(\mathcal{N})$ of a point set is therefore the result of removing the longest edge on each obtuse triangle from the original Delaunay tessellation $\mathrm{DT}(\mathcal{N})$, if this is not a

boundary edge. Since no new edges are generated in ADT($\mathcal{N}$), each triangle $f \in \mathcal{F}_{\mathrm{DT}}$ is part of some polygon $g \in \mathcal{F}_{\mathrm{ADT}}$. For detailed studies on quality measures and the application of the adaptive Delaunay tessellation we refer to Constantiniu et al. [12].

A constrained adaptive Delaunay tessellation (CADT) of the point set $\mathcal{N}$ is an extension of the ADT($\mathcal{N}$) that also confirms to constraints $\mathcal{C}$. In 2d, $\mathcal{C}$ is a given planar straight line graph which consists of a subset of $\mathcal{N}$ with its connecting edges, called constraining edges $e^{\mathcal{C}}$, that can intersect other edges e only at their end points. The method is based on the concepts from constrained Delaunay tessellation (CDT) that includes $e^{\mathcal{C}}$ which meet the Delaunay criterion as good as possible [42]. Hence, constrained edges are not necessarily Delaunay edges, the triangles f also do not necessarily fulfill the empty circumcircle property but they fulfill a weaker empty constrained circumcircle property. To state this property, it is convenient to think of constrained edges as blocking the view. Then, a tessellation is constrained Delaunay if any circumcircle $c(f)$ includes in its interior no other Delaunay visible vertices than its own, see Figure 2 [59]. Various algorithms are available for constructing an CDT, these include divide and conquer algorithms [8], sweep line algorithms [42] and incremental algorithms [61].
A tessellation is sought that contains the vertices in $\mathcal{N}$ and respects the constraining edges $e^{\mathcal{C}}$ [15]. A triangle $f(\mathcal{N})$ is constrained Delaunay, if f respects all constraints $\mathcal{C}$, which are fulfilled if $f \subset \mathcal{F}_{\mathrm{DT}}$, no e_f does intersect any constraining edge $e^{\mathcal{C}}$ or is a constraining edge itself, and there is a circumcircle $c(f)$ such that no other vertex of $\mathcal{N}$ is Delaunay visible, compare [59, Lemma 1]. If this is fulfilled for all f and with $\mathcal{E}^{>}$, the tessellation of the domain CH($\mathcal{N}$) represented by the sets $(\mathcal{F}_{\mathrm{CADT}}, \mathcal{E}_{\mathrm{CDT}} \setminus \mathcal{E}^{>})$ is called the constrained adaptive Delaunay tessellation CADT($\mathcal{N}$), where $\mathcal{F}_{\mathrm{CADT}}$ is the set of polygons generated by merging triangles with common edge in $\mathcal{E}^{>}$. Thus, the CADT($\mathcal{N}$) is the result of removing from each obtuse triangle $f^{>} \in \mathcal{F}_{\mathrm{CDT}}(\mathcal{N})$ the longest edge, if this is not a boundary or constrained edge. Since no new edges are generated in CADT($\mathcal{N}$), each triangle $f \in \mathcal{F}_{\mathrm{CDT}}$ is also part of some polygon $g \in \mathcal{F}_{\mathrm{CADT}}$. Figure 3 compares the initial CDT with the final CADT meshes for a non-convex domain.

4 Conforming interpolants on polygons

Here we reiterate the procedure for obtaining shape functions on cannonical polygonal domains. These are then combined with an affine map to evaluate the functions on convex and non-convex polygonal physical domains. We consider a polygonal domain $\Omega_0 \subset \Re^2$ defined by the set of n nodes defining the vertices of the polygon. $\boldsymbol{p}_K$ denote the K^{th} node, with coordinates $\boldsymbol{p}_K \equiv (x_k, y_k)$. Any point with coordinate $\boldsymbol{p} \equiv (x, y) \in \Omega_0$ has a set of associated shape functions $\phi_K(\boldsymbol{p})$. An interpolation scheme for a scalar-valued function $u(\boldsymbol{p}) : \mathcal{B}_0 \to \Re^2$ can be written as:

$$u^h(\boldsymbol{p}) = \sum_{K=1}^{n} \phi_K(\boldsymbol{p}) u_K \tag{11}$$

where u_K are the unknowns at the n nodes of the polygon. The function $u^h(\boldsymbol{p})$ satisfies properties such as partition of unity, interpolation and linear completeness inside the polygon and on the boundaries. We use various geometric measures like edge length, signed area, and sine or cosine of the angles at each vertex of the polygon to construct the interpolants as discussed below.

4.1 Malsch Interpolant

Malsch and Dasugupta ([29] , [28], [30], [45]) have presented a rational procedure for constructing smooth and bounded interpolants on both convex and concave polygons. The interpolant is expressed as:

$$\phi_I^M(\boldsymbol{p}) = \frac{k_I s_I(\boldsymbol{p})}{\sum_{J=1}^{n} k_J s_J(\boldsymbol{p})} \tag{12}$$

Where $s_I(\boldsymbol{p})$ are defined as the helper functions that accounts for adjacency and k_I is any arbitrarily chosen constant. Appropriate choices of the helper function and constants are made so as to ensure the interpolation requirements along boundaries and any interior points present within the polygonal domain. With reference to Figure 4 , one can define s_I as product of functions that are zero along all the boundary segments from node $I+1$ to node $I-1$, that are adjacent to node I. This can be written as:

$$s_I(\boldsymbol{p}) = \prod_{I \neq I-1 \& I \neq I+1} r_{I+1,I-1}(\boldsymbol{p}) \tag{13}$$

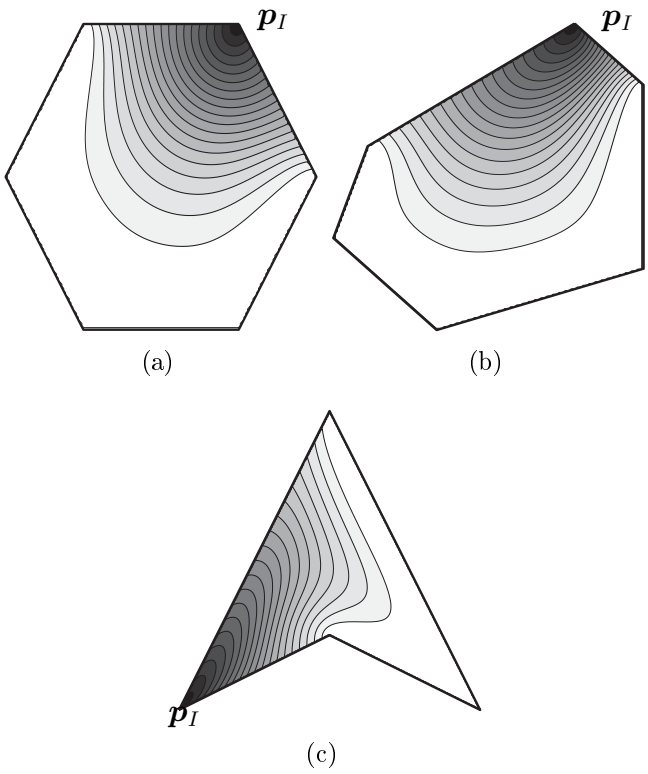

Figure 6: a) Malsch interpolant on a canonical hexagon b) Malsch interpolant on a physical polygon c) Malsch interpolant on a concave polygon

For convex polygons the function $r_{I+1,I-1}(\boldsymbol{p}) = A(\boldsymbol{p}, \boldsymbol{p}_I, \boldsymbol{p}_{I+1})$ and $k_I = A(\boldsymbol{p}_I, \boldsymbol{p}_{I+1}, \boldsymbol{p}_{I-1})$. For concave polygons $r_{I+1,I-1}(\boldsymbol{p}) = l_{I+1}(\boldsymbol{p}) + l_{I-1}(\boldsymbol{p}) - l_{I+1,I-1}$ and $k_I = 1$. Here the length measure is defined as $l_I = ((x - x_I)^2 + (y - y_I)^2)^{0.5}$ and $l_{I,I+1} = ((x_I - x_{I+1})^2 + (y_I - y_{I+1})^2)^{0.5}$.

The Malsch interpolation over a canonical and physical polygon are shown in Figure 6a and Figure 6b. The interpolation over an concave polygon is shown in Figure 6c.

5 Discretized weak form and numerical integration

Herein we use the polygonal interpolant both for the deformation map and for the space of admissible variations.

$$\boldsymbol{\varphi}^h(\boldsymbol{p}) = \sum_{k=1}^{n} \phi^k(\boldsymbol{p})\boldsymbol{\varphi}^k \tag{14}$$

$$\delta\boldsymbol{\varphi}^h(\boldsymbol{p}) = \sum_{k=1}^{n} \phi^k(\boldsymbol{p})\delta\boldsymbol{\varphi}^k \tag{15}$$

where $\phi^k(\boldsymbol{p})$ and are the shape functions for the node k that are associated with nodal deformations $\boldsymbol{\varphi}^k$, Herein, the nodal indices k account for the discrete values of the unknown $\boldsymbol{\varphi^h}$. These shape functions have the interpolating property. The first order deformation gradients are defined as

$$\boldsymbol{F}^h = \sum_{k=1}^{n} \boldsymbol{\varphi}^k \otimes \nabla_X \phi^k \tag{16}$$

In order to obtain the discretized spatial equilibrium equations, recall the principle of virtual work. Introducing the interpolation for $\delta\boldsymbol{\varphi}$ we have

$$\delta\Pi(\boldsymbol{\varphi}^h; \delta\boldsymbol{\varphi}^k) = \int_{B_0} \boldsymbol{P}(\boldsymbol{\varphi}^h) : \left[\sum_{k=1}^{n} \delta\boldsymbol{\varphi}^k \otimes \nabla_X \phi^k\right] dV \tag{17}$$
$$+\delta\Pi^{ext}(\delta\boldsymbol{\varphi}^h)$$

The above equation can be rearranged for all $\delta\boldsymbol{\varphi}^k$ as

$$\delta\Pi(\boldsymbol{\varphi}^h; \delta\boldsymbol{\varphi}^k) = \sum_{k=1}^{n} \delta\boldsymbol{\varphi}^k \cdot \int_{\mathcal{B}_0} \left[\boldsymbol{P}(\boldsymbol{\varphi}^h) \cdot \nabla_X \phi^k\right] dV \tag{18}$$
$$+\delta\Pi^{ext}(\delta\boldsymbol{\varphi}^h) = \boldsymbol{0}$$

The discrete residual can thus be written as

$$\boldsymbol{R}_k = \int_{\mathcal{B}_0} \boldsymbol{P}(\boldsymbol{\varphi}^h) \cdot \nabla_X \phi^k(\boldsymbol{p}) dV - \boldsymbol{F}_k^{ext} = 0 \tag{19}$$

This represents a set of nonlinear equilibrium equations with the current nodal deformation as unknowns. The solution of these equations is achieved using a Newton Raphson iterative procedure. The linearized problem is given by

$$\sum_{l=1}^{n} \left[\boldsymbol{K}_{kl}\right] \left[d\boldsymbol{\varphi}^l\right] = \left[\boldsymbol{F}_k^{ext} - \boldsymbol{F}_k^{int}\right] \tag{20}$$

and is solved for iterative increments of $\boldsymbol{\varphi}^l$ The component matrices of the global tangent stiffness matrix are given by

$$\boldsymbol{K}_{kl} = \frac{\partial \boldsymbol{R}_k}{\partial \boldsymbol{\varphi}_l} = \int\limits_{\mathcal{B}_0} \left[\partial_F \boldsymbol{P} \cdot \nabla_X \phi^k\right] \cdot \nabla_X \phi^l dV \tag{21}$$

where the tangent operators for the specific constitutive law read as

$$\partial_F \boldsymbol{P} = \lambda \boldsymbol{F}^{-T} \otimes \boldsymbol{F}^{-T} - [\lambda \ln J - \mu]\, \boldsymbol{F}^{-T} \underline{\otimes} \boldsymbol{F}^{-T} + [\mu]\, \boldsymbol{I} \overline{\otimes} \boldsymbol{I} \tag{22}$$

Here $\boldsymbol{K}_{kl}$ is a tensor of second order arranged in appropriate global locations to yield the global stiffness matrix.

Numerical integration of the Galerkin weak form is required to be performed over the polygonal domain for evaluating the integrals. Standard Gaussian integration rule is used for finite elements and for mesh free methods based on back ground cells. Presently the state of the art includes the following methods for performing numerical integration over polygonal domains:

- Integration on the physical polygonal element $n-gon$ by subdividing it in to n triangles and then using standard quadrature rule on triangles [12], [48].
- Partitioning the canonical (regular) polygonal element $n-gon$ into n triangles and then performing numerical quadrature on triangles [48].
- Cubature rules for irregular $n-gons$ [16] [17] based on triangles [54] [56] or conformal mapping [34], [35], [25].
- Generalized quadratures rules [27] on triangles or polygons based on symmetry groups and numerical optimization [43], [33] [26]and [58].

In the present work we apply for simplicity the first two approaches. In performing the numerical integration by partitioning of the physical element, the integration of a (scalar) function ψ over $\mathcal{B}_i$ (a $n-gon$) is written as

$$\int_{\mathcal{B}_i} \psi d\mathcal{B} = \sum_{j=1}^{n} \int_{\mathcal{B}_i^{\triangle_j}} \psi d\mathcal{B} = \sum_{j=1}^{n} \int_0^1 \int_0^{1-\xi} \psi \mid \mathbf{J}^j \mid d\xi d\eta \tag{23}$$

A nsp quadrature rule on each of the reference triangles is used to compute the last integral. In the above case for a given quadrature point we determine

$\mathbf{X}$ via : $\mathbf{X} = \sum_{i=1}^{3} \phi^a \mathbf{X}^a$. Where ϕ^a are the finite element shape functions for a three node triangle. To compute the Malsch shape functions we need the ξ coordinates in the canonical element. The position in physical coordinates are obtained by inverse mapping [47].

Any N-gonal domain may be decomposed into N pairwise disjoint triangular subdomains $\bar{\Omega}$ and then any integration of a function ψ on a physical domain Ω can be written as

$$\int_{\Omega} \psi \; d\Omega = \sum_{N} \int_{\bar{\Omega}} \psi \; d\bar{\Omega} \tag{24}$$

$$= \sum_{N} \int_{\bar{\Omega}_0} \psi \; |\boldsymbol{J}| \; d\bar{\Omega}_0 \tag{25}$$

$$= \sum_{N} \int_{\bar{\Omega}_\triangleleft} \psi \; |\boldsymbol{J}||\boldsymbol{J}_\triangleleft| \; d\bar{\eta} \; d\bar{\xi} \tag{26}$$

and thereby be pulled back for integration either on a triangle in the canonical domain Ω_0 or a generic triangular domain $\Omega_\triangleleft$. (24)-(26) may individually be integrated with any adequate quadrature scheme. We select classical 2D Gaussian quadrature defined on a generic triangular domain with $n_\triangleleft^{\mathrm{G}}$ quadrature points on each of the N subdomain triangles. For the application of (24) and (25) the Gauss points $\boldsymbol{p}_\triangleleft^{\mathrm{G}}$ and the associated weights w^{G} can also be mapped into the appropriate domains Ω or Ω_0, respectively.

6 Numerical examples

6.1 Square plate with a central hole

In a square specimen of side length $L = 2\,in$, an inhomogeneity is introduced by means of a centered circular hole of radius $r = 1\,in$, as shown in Figure 7. The nodes at the bottom edge of the discretized geometry are fixed in vertical direction, a constant displacement boundary condition in the same direction is applied on the top nodes step wise, until the final length of $1.5L$ is reached. Lamé constants of $\lambda = 73.5$ GPa, $\mu = 36.5$ GPa , resulting in a Poisson ratio of $\nu = 0.25$ are considered.

The square specimen with central hole is first discretized with randomly generated Delaunay triangles. The proposed CADT algorithm and code is then used to generate the CADT polygonal mesh as shown in Figure 8(c). The small amount of asymmetry in the polygonal discretization may be attributed to the randomness in the Delaunay tessellation that is initially considered for CADT. For a comparative study the square specimen with hole

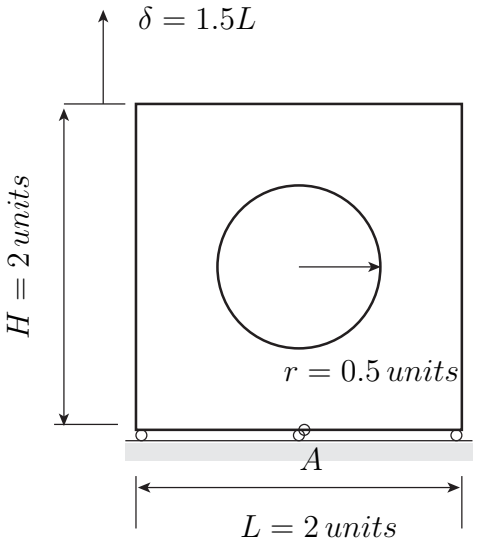

Figure 7: Square plate with a circular hole.

is also discretized using three noded triangular elements as shown in Figure 8(a). A hyperelastic analysis is performed and the final deformed meshes are shown in Figure 8(b) and 8(d) . A quadratic convergence is achieved in both cases. Polygonal elements with n sides offer more flexibility than regular three noded triangular elements especially for large deformations. Further more the advantage of a ADT mesh at large deformations is that a triangular element present in an ADT mesh that tends to be too elongated can be merged with other triangles to form a n sided polygon in a CADT mesh. The stresses are computed for hyper- elastic analysis. Stress smoothing by nodal averaging is performed at the nodes of the polygonal elements. Figure 9(a), (b) and (c) indicate the stress plots σ_{xx}, σ_{yy} and σ_{xy} for the polygonal discretization. It is observed from Figure 10 that at large deformations for the same amount of applied displacement, the reaction force measured is less in the polygonal finite element method than in the classical FEM approach thus clearly indicating that it is a more flexible discretization.

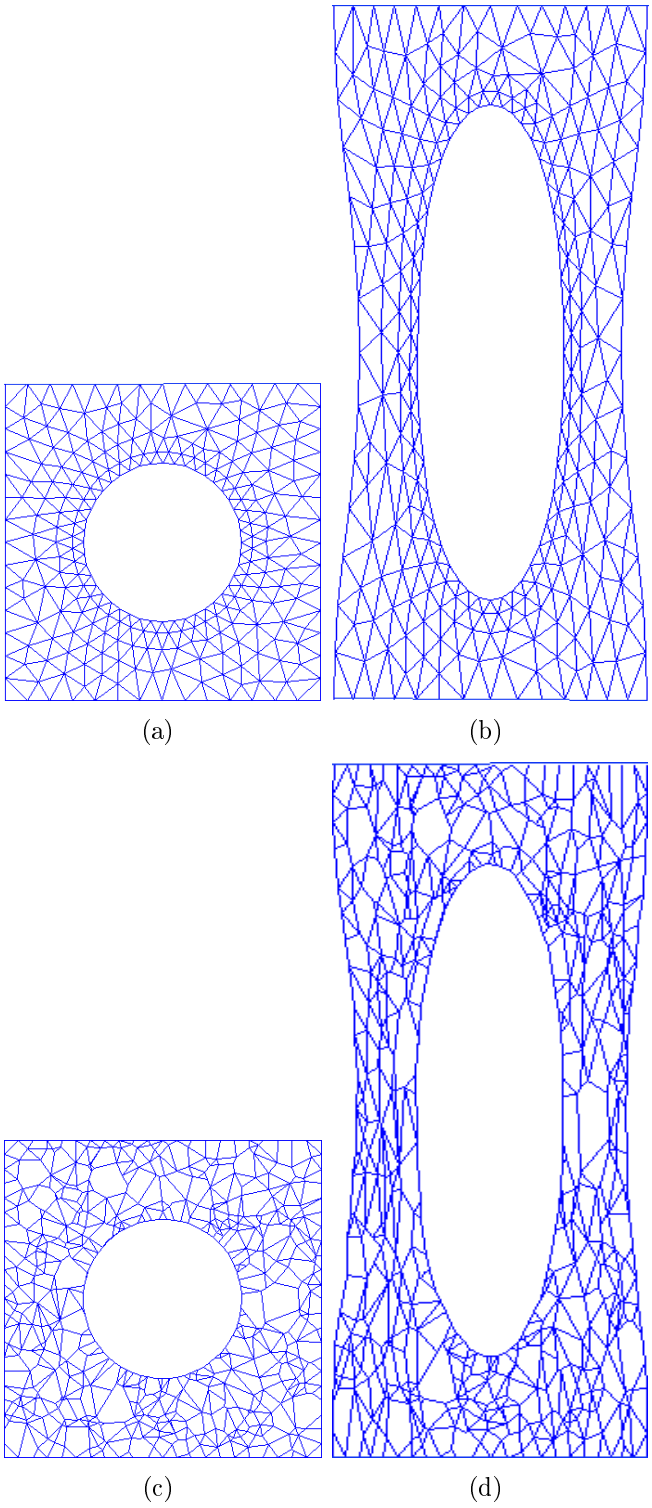

Figure 8: Hyperelastic analysis of a unit square domain with a central hole with restraint at the bottom edge and a prescribed displacement on the top edge a) Initial configuration using a FEM discretization based on a three noded triangular elements b)Final configuration using a FEM discretization based on three noded triangular elements c) Initial configuration using a CADT polygonal discretization d) Final configuration using a CADT polyg-

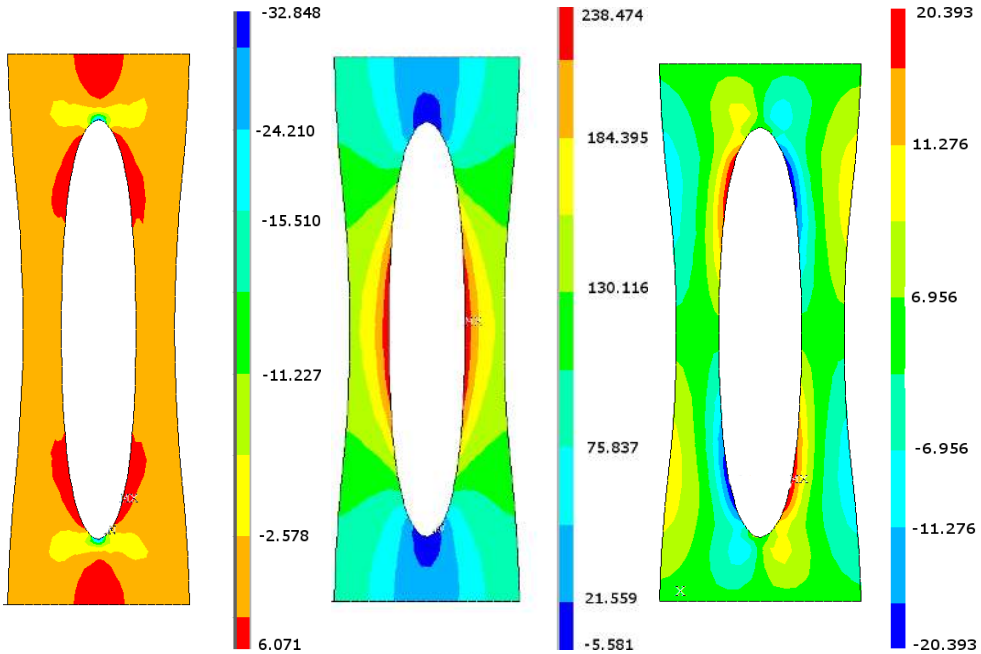

(a) (b) (c)

Figure 9: Stress distribution for unit square domain with a central hole corresponding to the CADT mesh (shown in Figure 8d) a) Stress σ_{xx} b) Stress σ_{yy} c) Stress σ_{xy}.

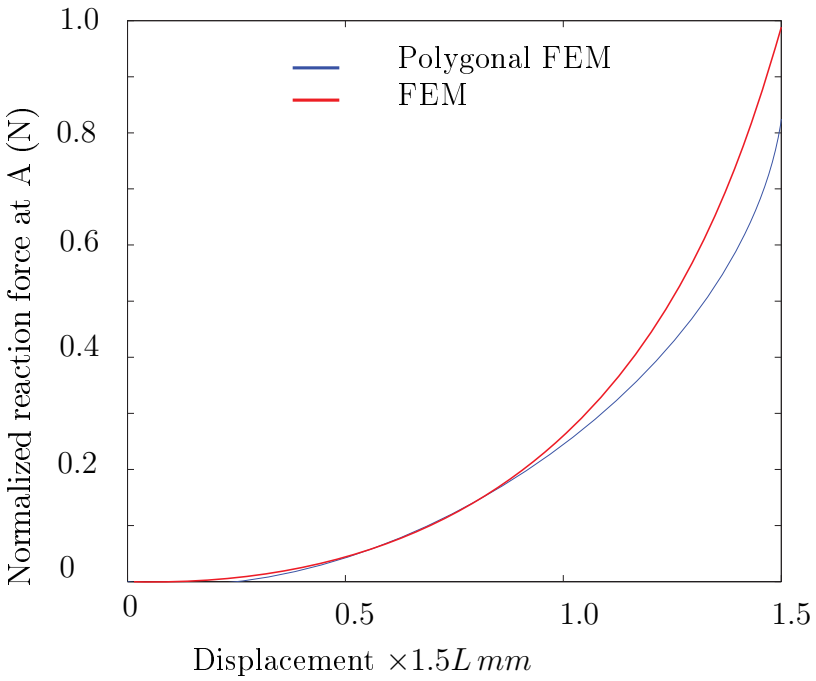

Figure 10: Reaction force versus displacement plot for plate with a hole example.

6.2 L shaped domain

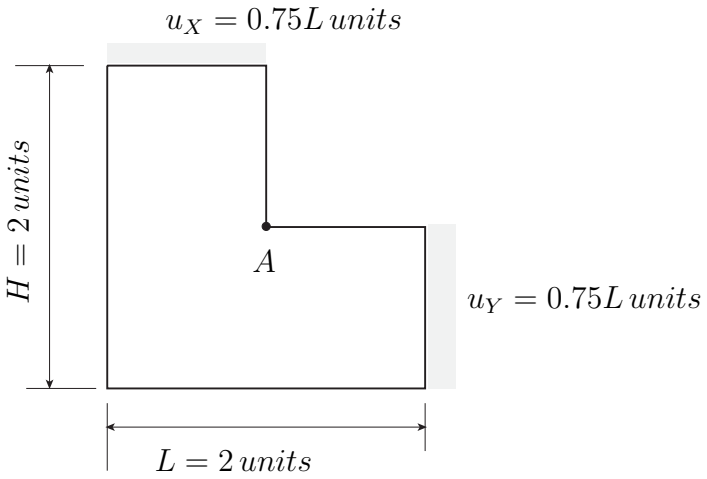

(a)

Figure 11: L- shaped domain

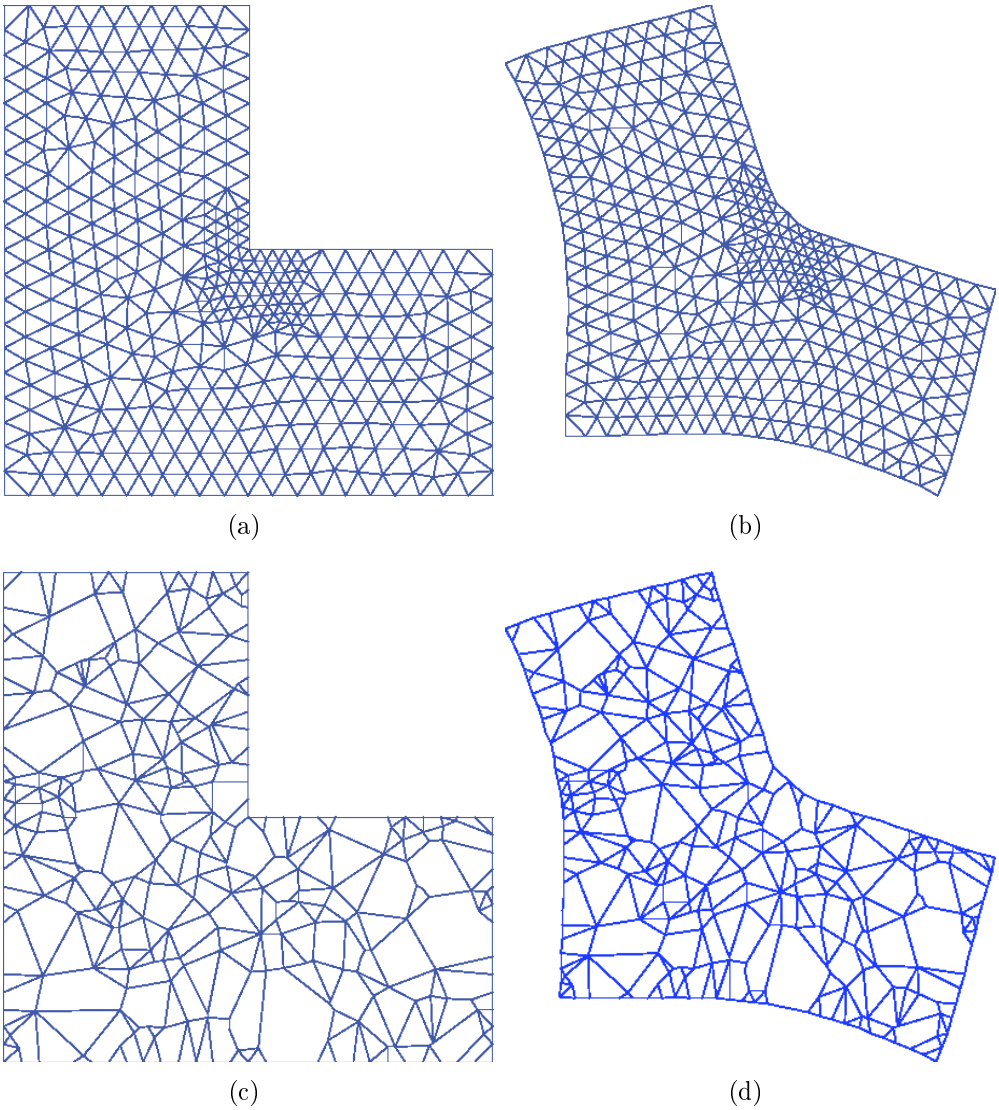

Figure 12: Hyperelastic analysis on a L shaped domain with restraint at the renentrant corner and prescribed displacements in axial direction along the two legs. a) Initial configuration using a FEM discretization based on three noded triangular elements b) Final configuration using a FEM discretization based on three noded triangular elements c) Initial configuration using a CADT polygonal discretization d) Final configuration using a CADT polygonal discretization

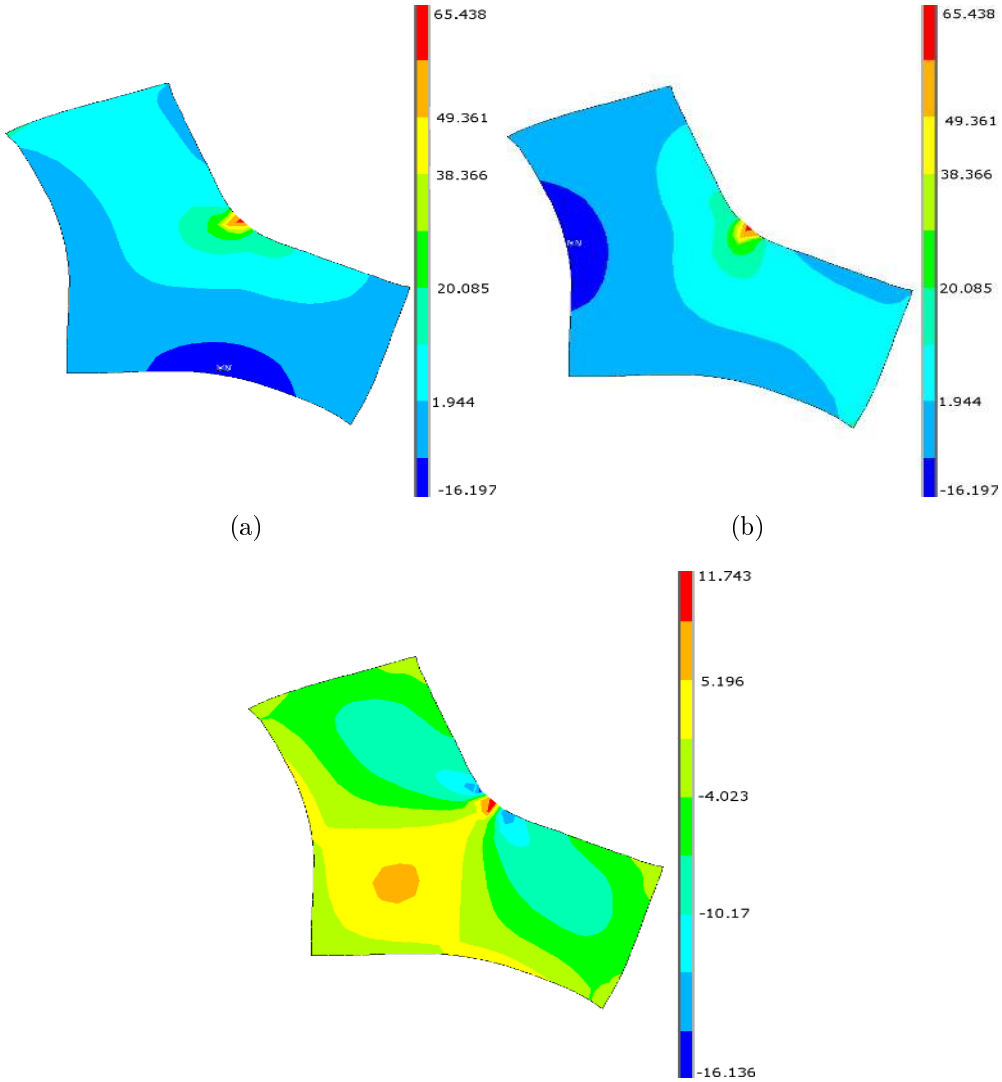

Figure 13: Stress distribution for an L shaped domain. The results obtained are for CADT mesh shown in Figure 12d. a)Stress σ_{xx} b) Stress σ_{yy} c) Stress σ_{xy}

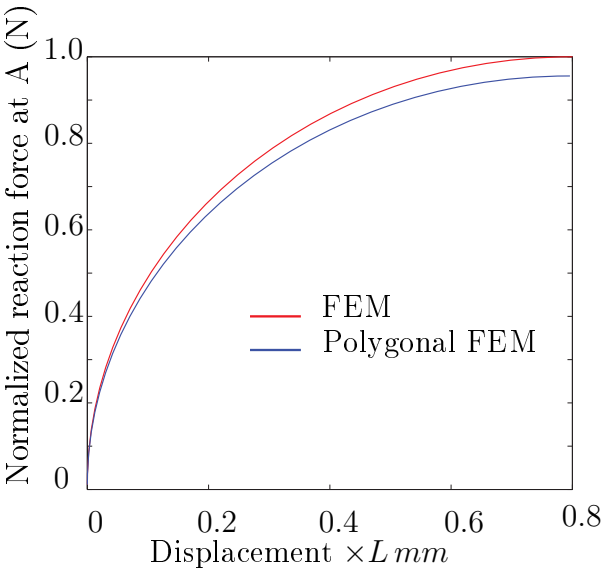

Figure 14: Reaction force versus diplacement plot for L-shaped example.

A L-shaped specimen of the dimensions as shown in Figure 11 is considered. The specimen is subjected to a prescribed displacement in the X and Y direction along the two legs. To prevent rigid body motion all the deformation degrees of freedom at the re-entrant corner A are additionally fixed. The Lamé constants are taken as $\lambda = 73.5$ GPa, $\mu = 36.5$ GPa resulting in a Poisson's ratio $\nu = 0.25$. The proposed CADT algorithm is then used to generate the CADT polygonal mesh as shown in Figure 12(c). For a comparative study the L- shaped specimen is also discretized using three noded triangular elements as shown in Figure 12(a). A hyper-elastic analysis is performed and the final deformed meshes are shown in Figure 12(b) and 12(d). A quadratic convergence is achieved in both cases. Stress smoothing by nodal averaging is performed at the nodes of the polygonal element . Figure 13(a),(b) and (c) indicate the stress plots σ_{xx}, σ_{yy} and σ_{xy} for the polygonal discretization. It is observed from Figure 14 that at large deformations for the same amount of applied displacement, the reaction force measured is less in polygonal finite element method than the classical FEM approach thus clearly indicating that it is a more flexible discretization. This may be attributed the increased number of degrees of freedom per element for polygonal FEM discretization and to the flexible interpolation schemes used in the polygonal FEM.

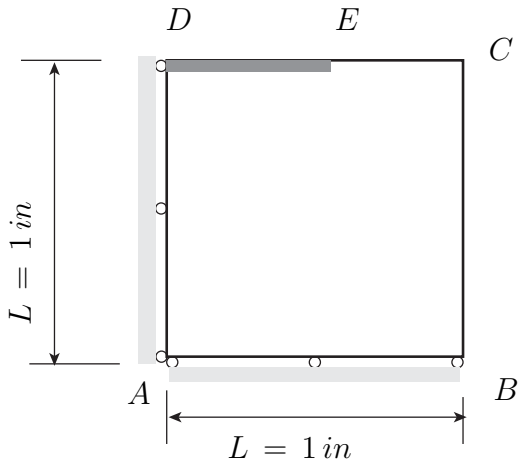

Figure 15: Square block under compression.

6.3 Square block under compression

A square block of dimensions as shown in Figure 15 is subjected to a non uniform compression. Displacements are applied along DE so as to induce non uniform compression. Symmetric boundary conditions are applied along AD and AB. Because of the symmetry, only one-half of the block is considered for convenience. The proposed CADT algorithm is then used to generate the CADT polygonal mesh as shown in Figure 16(c). For a comparative study the square block under compression is also discretized using three noded triangular elements as shown in Figure 16(a). A hyper-elastic analysis is performed and the final deformed meshes are shown in Figure 16(b) and 16(d). A quadratic convergence is achieved in both cases. Stress smoothing by nodal averaging is performed at the nodes of the polygonal elements. Figure 17(a),(b) and (c) indicate the stress plots σ_{xx}, σ_{yy} and σ_{xy} for the polygonal discretization. It is observed from Figure 18 that at large deformations for the same amount of applied displacement, the reaction force measured is less in the polygonal finite element method than in the classical FEM approach, thus clearly indicating that it is a more flexible discretization.

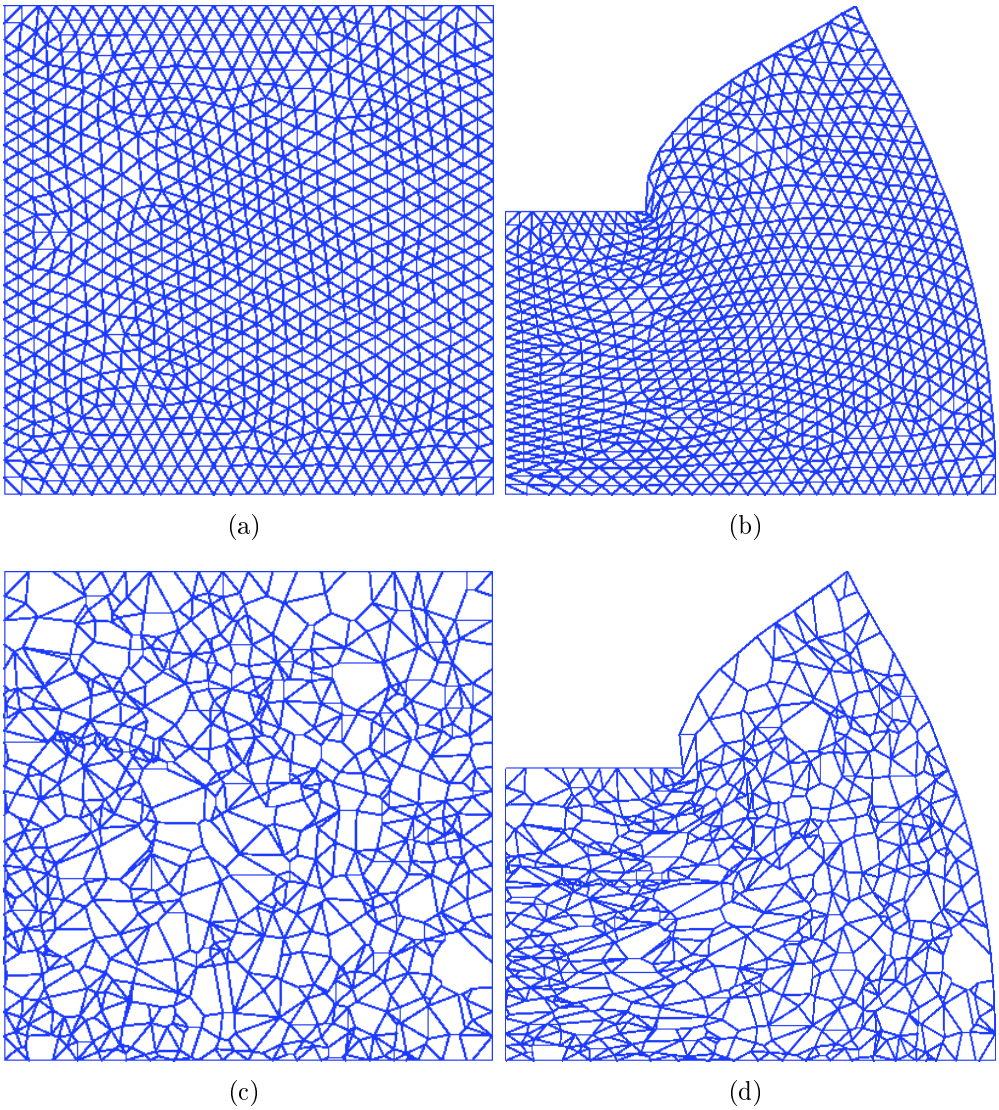

Figure 16: Hyperelastic analysis on a unit square domain subjected to compression with restraint at the bottom edge and a prescribed displacement on the top edge. a) Initial configuration using a FEM discretization based on three noded triangular elements b)Final configuration using a FEM discretization based on three noded triangular elements c) Initial configuration using a CADT polygonal discretization d) Final configuration using a CADT polygonal discretization

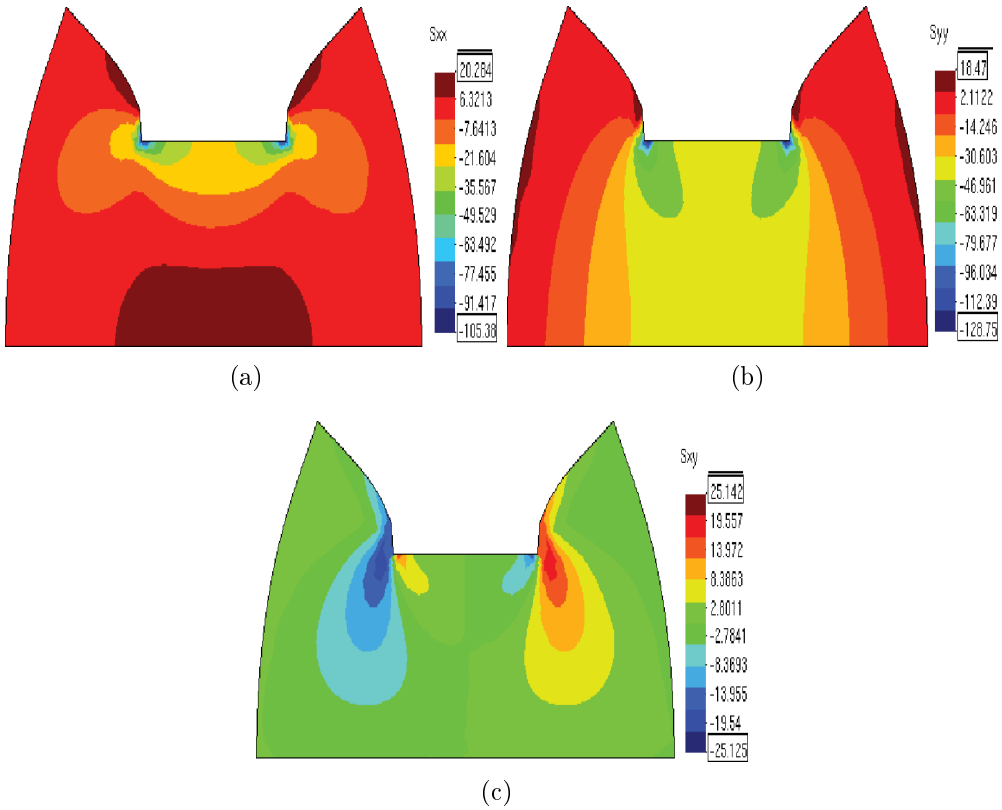

(a) (b)

(c)

Figure 17: Stress plots for the unit square domain subjected to compression. The results are obtained for CADT meshes (shown in Figure16d). a) Stress σ_{xx} b) Stress σ_{yy} c) Stress σ_{xy}

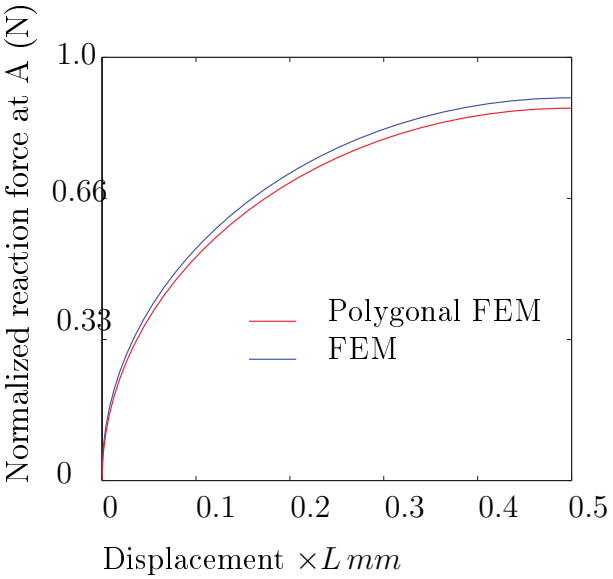

Figure 18: Reaction force versus diplacement plot for block example.

7 Summary and Conclusions

In this work, we present a procedure for hyperelastic analysis using a novel polygonal finite element method based on Constrained Adaptive Delaunay Tessellation (CADT). For generating polygonal meshes we use the Adaptive Delaunay Tessellation (ADT). ADT is an unstructured hybrid tessellation of a scattered point set that minimally covers the proximal space around each point. In this work, we have extended the ADT for non-convex domains using concepts from Constrained Delaunay Triangulation. We have used the Malsch interpolant for approximation over polygonal regions. For numerical integration of the Galerkin weak form we resort to classical Gaussian quadrature rules based on triangles. In the numerical examples, we have implemented a plate with square hole, a L-shaped domain and a block under compression. Polygonal elements with n sides offer more flexibility than regular three nodded triangular elements especially for large deformations. Also the advantage of an ADT mesh at large deformations is that a triangular element present in a ADT mesh that tends to be too elongated can be merged with other triangles to form $n-$ sided polygons in a CADT mesh. The present method compares well with the results obtained from classical FEM, as observed in the deformation patterns that are obtained.

References

[1] Andrew Gillette, A. R. & C. Bajaj [2012]. 'Error estimates for generalized barycentric interpolation.' *Advances in Computational Mathematics*, **37**(3), pp. 417–439.

[2] Arun, L. G., C. Talischi & G. H. Paulino [2014]. 'On the virtual element method for three-dimensional linear elasticity problems on arbitrary polyhedral meshes.' *Computer Methods in Applied Mechanics and Engineering*, **282**, pp. 132–160.

[3] Barros, F. B., S. D. Barcellos & C. A. Durate [2007]. 'p adaptive c^k generalized finite element for arbitrary polygonal clouds.' *Journal of Numerical Mathematics*, **41**, pp. 175 – 187.

[4] Biabanaki, S. O. R. & A. R. Khoei [2012]. 'A polygonal finite element method for modeling arbitrary interfaces in large deformation problems.' *Computational Mechanics*, **50**, pp. 19–33.

[5] Biabanaki, S. O. R., A. R. Khoei & P. Wriggers [2014]. 'Polygonal finite element methods for contact-impact problems on non-conformal meshes.' *Computer Methods in Applied Mechanics and Enginnering*, **269**, pp. 198–221.

[6] Bobach, T., A. Constantiniu, P. Steinmann & G. Umlauf [2010]. 'Geometric properties of the adaptive Delaunay tessellation.' *Lect Notes Comput Sci*, **5862**, pp. 41–54.

[7] Calvo, N., S. R. Idhelson & E. Onate [2003]. 'The extended Delaunay tessellation.' *Engineering Computations*, **20(5/6)**, pp. 583 – 600.

[8] Chew, L. P. [1989]. 'Constrained Delaunay triangulations.' *Algorthimica*, **4(1)**, pp. 97 – 108.

[9] Chi, H., C. Talischi, L. P. Oscar & G. H. Paulino [2015]. 'Polygonal finite elements for finite elasticity.' *International Journal for Numerical Methods in Engineering*, **101**, pp. 305–328.

[10] Chiong, I. & C. Song [2010]. 'Development of polygonal elements based on the scaled boundary finite element.' *WCCM/APCOM2001:*

Material Science and Engineering, **10**, pp. doi: 10.1088/1757–899X/10/1/012226.

[11] Chunmei, W. & W. Junping [2014]. 'An efficient numerical scheme for the biharmonic equation by weak Galerkin finite element methods on polygonal or polyhedral meshes.' *Computers and Mathematics with Applications*, **68**(12), pp. 2314–2330.

[12] Constantinu, A., P. Steinmann, T. Bobach, G. Farin & G. Umlauf [2008]. 'The adaptive Delaunay tessellation : A neighborhood covering meshing technique.' *Computational Mechanics*, **42**(5), pp. 655 – 669.

[13] Dai, K. Y., G. R. Liu & T. T. Nguyen [2007]. 'An n-sided polygonal smoothed finite element method (nSFEM) for solid mechanics.' *Finite elements in Analysis and Design*, **43(11-12**, pp. 847 – 860.

[14] David, C. & H. K. Nancy [2014]. 'Generation of polyhedral delaunay meshes.' *Procedia Engineering*, **82**, pp. 291–300.

[15] De, F. L. & E. Puppo [1992]. 'An online algorithm for constrained Delaunay triangulation.' *CVGIP: Graphical Models and Image Processing*, **54(3)**, pp. 290 – 300.

[16] De, S. & K. J. Bathe [2000]. 'The method of finite spheres.' *Computational Mechanics*, **25(1)**, pp. 329 – 345.

[17] De, S. & K. J. Bathe [2001]. 'The method of finite spheres with improved numerical integration.' *Computers and Structures*, **79(22)**, pp. 2183 – 2196.

[18] Dohrmann, C. R., S. W. Key & M. W. Heinstein [2000]. 'A method for connecting dissimilar finite element meshes in two dimensions.' *International Journal for Numerical methods in Engineering*, **48(5)**, pp. 655 – 678.

[19] Floater, M. [2003]. 'Mean value coordinates.' *Computer Aided Geometric Design*, **20**, pp. 19 – 27.

[20] Gosh, S. & S. Moorthy [1995]. 'Elastic plastic analysis of arbitrary heterogeneous materials with the Voronoi cell finite element method.'

Computer Methods in Applied Mechanics and Engineering, **121**(1-4), pp. 373–409.

[21] Hornmann, K. & N. Sukumar [2009]. 'Maximum Entropy coordinates for arbitrary polytopes.' *Eurographics Symposium on Geometry Processing 2008*, **27**(5), pp. 1–12.

[22] Kraus, M. & P. Steinmann [2012]. 'Finite element formulations for 3D convex polyhedra in nonlinear continuum mechanics.' *Computer Assisted Methods in Engineering and Sciences*, **19**, pp. 121–134.

[23] Kuznetsov, Y. A. [2006]. 'Mixed finite element method for diffusion equations on polygonal meshes with mixed cells.' *Journal of Numerical Mathematics*, **14(4)**, pp. 305 – 315.

[24] Li, C. J., P. Lamberti & C. Dagnino [2009]. 'Numerical integration over polygons using an eight-node quadrilateral spline finite element.' *Journal of Computational and Applied Mathematics*, **233**, pp. 279 – 292.

[25] Lin, B. & S. N. Chandlerwilde [2000]. 'Numerical conformal mapping and mesh generation for polygonal and multiply connected regions.' *Journal of Hydro Informatics*, **2(4)**, pp. 255 – 266.

[26] Lyness, J. N. & D. Jespersen [1975]. 'Moderate degree symmetric quadrature rule for triangles.' *Journal of the Institute of Mechanics and its Applications*, **15**, pp. 19 – 32.

[27] Ma, J., V. Rokhlin & S. Wandzura [1996]. 'Generalized quadrature of systems of arbitrary functions.' *SIAM journal on Numerical Analysis*, **33(3)**, pp. 971 – 996.

[28] Malsch, E. A. & G. Dasgupta [2004]. 'Interpolation constraints and thermal distributions: a method for all non-concave polygons.' *International Journal of Solids and Structures*, **41(8)**, pp. 2165 – 2188.

[29] Malsch, E. A. & G. Dasgupta [2004]. 'Shape functions for polygonal domains with interior nodes.' *International journal for Numerical Methods in Engineering*, **61**, pp. 1153 – 1172.

[30] Malsch, E. A., J. J. Lin & G. Dasgupta [2005]. 'Smooth two dimensional interpolations : A recipe for all polygons.' *Journal of Graphics, GPU and Game tools*, **10(2)**, pp. 27 – 39.

[31] Manzini, G., A. Russo & N. Sukumar [2014]. 'Gradient bounds for Wachspress coordinates on polytopes.' *SIAM Journal of Numerical Analysis*, **52**(1), pp. 515–532.

[32] Manzini, G., A. Russo & N. Sukumar [2014]. 'New perspectives on polygonal and polyhedral finite element methods.' *Mathematical Models and Methods in Applied Sciences*, **24**(8), pp. 1665–1699.

[33] Mousavi, S. E., H. Xiao & N. Sukumar [2009]. 'Generalized Gaussian quadrature rules on arbitrary polygons.' *International Journal for Numerical Methods in Engineering*, **82(1)**, pp. 99 – 113.

[34] Natarajan, S., S. Bordas & D. R. Mahapathra [2009]. 'Numerical integration over arbitrary polygonal domains based on Schwarz -Christoffel conformal mapping.' *International Journal of Numerical Methods in Engineering*, **80(1)**, pp. 103 – 134.

[35] Natarajan, S., S. Bordas & D. R. Mahapathra [2010]. 'Integrating strong and weak discontinuities without integration sub cells and example applications in XFEM/GFEM framework.' *International Journal of Numerical Methods in Engineering*, **83(3)**, pp. 269 – 294.

[36] Natarajan, S., E. T. Ooi, I. Chiong & C. Song [2014]. 'Convergence and accuracy of displacement based finite element formulations over arbitrary polygons:laplace interpolants,strain smoothing and scaled boundary polygon formulation.' *Finite Elements in Analysis and Design*, **85**, pp. 101–122.

[37] Nguyen Thoi, T., H. Nguyen Xuan, P. Phung Van, T. Rabczuk & C. Le Van [2013]. 'Free and forced vibration analysis using the n-sided polygonal cell-based smoothed finite element method (nCS-FEM).' *International Journal of Computational Methods*, **10**(1), pp. 1–19.

[38] Rashid, M. M. & P. M. Gullett [2000]. 'On a finite element method with variable element topology.' *Computer Methods in Applied Mechanics and Engineering*, **190**, pp. 1509 – 1527.

[39] Rjasanow, S. & S. Weiber [2012]. 'Higher order BEM-based FEM on polygonal meshes.' *Society for Industrial and Applied Mathematics*, **50**(5), pp. 2357–2378.

[40] Sayas, F. J. [2013]. 'The validity of johnson–nedelec's BEM–FEM coupling on polygonal interfaces.' *Society for Industrial and Applied Mathematics*, **55**(1), pp. 131–146.

[41] Schewchuk, J. [2002]. 'What is a good linear element? interpolation, conditioning and quality measures.' *Proceedings, 11th International meshing round table conference*, **LNCS 5862**, pp. 115 – 126.

[42] Shewchuk, J. R. [2008]. 'General dimensional constrained Delaunay and constrained regular triangulations i : Combinatorial properties.' *Discrete and Computational Geometry*, **39(1-3)**, pp. 580 – 637.

[43] Silvester, P. [1970]. 'Symmetric quadrature formula for simplexes.' *Mathematics of Computations*, **24**, pp. 95 – 100.

[44] Sukumar, N. [2013]. 'Quadratic maximum-Entropy serendipity shape functions for arbitrary planar polygons.' *Computational Methods in Applied Mechanics and Engineering*, **263**, pp. 27–41.

[45] Sukumar, N. & E. A. Malsch [2006]. 'Recent advances in construction of polygonal finite element interpolants.' *Archives of computational methods in engineering*, **13(1)**, pp. 129 – 163.

[46] Sukumar, N., G. Manzini & A. Russo [2000]. 'Hourglass stabilization and the virtual element method.' *International Journal for Numerical Methods in Engineering*, **1**, pp. 1–33.

[47] Sukumar, N. & J. H. Prevost [2003]. 'Modeling quasi static crack growth with the extended finite element method part i : computer implementation.' *International Journal of Solids and structures*, **40**, pp. 7513 – 7537.

[48] Sukumar, N. & A. Tabarraei [2004]. 'Conforming polygonal interpolants.' *International Journal of Numerical Methods in Engineering*, **61**, pp. 2045 – 2066.

[49] Sze, K. Y. & N. Sheng [2005]. 'Polygonal finite element method for nonlinear constitutive modeling of polycrystalline ferroelectrics.' *Finite Elements in Analysis and Design*, **42(2)**, pp. 107 – 129.

[50] Talischi, C., G. Paulino, A. Pereira & I. Menezes [2010]. 'Polygonal finite elements for topology optimization: A unifying paradigm.' *International Journal for Numerical Methods in Engineering*, **82**, pp. 671–698.

[51] Talischi, C., G. H. Paulino, A. Pereira & I. F. M. Menezes [2007]. 'Polygonal finite element for topology optimization : A unifying paradigm.' *International Journal for Numerical Methods in Engineering*, **82(6)**, pp. 671 – 698.

[52] Talischi, C., A. Pereira, G. H. Paulino, I. F. M. Menezes & M. S. Carvalho [2014]. 'Polygonal finite elements for incompressible fluid flow.' *International Journal for Numerical Methods in Fluids*, **74**(2), pp. 134–151.

[53] Tang, X. H., S. C. Wu, C. Zheng & J. H. Zhang [2009]. 'A novel virtual node method for polygonal elements.' *Appl. Math. Mech. -Engl. Ed.*, **30(10)**, pp. 1233 – 1246.

[54] Taylor, M. A. [2008]. 'Assymetric cubature formulas for polynomial integration in the triangle and square.' *Journal of Computational and Applied Mathematics*, **218**, pp. 184 – 191.

[55] Wachspress, E. L. [1975]. 'A rational finite element basis.' **New york, Academic press**.

[56] Wandzura, S. & H. Xiao [2003]. 'Symmetric quadrature rules on a triangle.' *Computers and Mathematics with Applications*, **45**, pp. 1829 – 1840.

[57] Warren, J., S. Shaefer, A. N. Hirani & M. Desbrun [2007]. 'Barycentric coordinates for convex sets.' *Advances in Computational Mathematics*, **27**, pp. 319 – 338.

[58] Xiao, H. & Z. Gimbutas [2010]. 'A numerical algorithm for construction of efficient quadrature rules in two and higher dimensions.' *Computers and Mathematics with Applications*, **59(2)**, pp. 663 – 676.

[59] Yang, Y. J., H. Zhang, J. H. Yong, W. Zeng, J. Paul & J. Sun [2006]. 'Constrained Delaunay triangulation using Delaunay visibility.' *Lecture notes in Computer Science*, **4291**, pp. 682 – 691.

[60] Yijiang, P., Z. Lijuan, P. Jiwei & G. Qing [2014]. 'A two-dimensional base force element method using concave polygonal mesh.' *Engineering Analysis with Boundary Elements*, **42**, pp. 45–50.

[61] Zalik, B. & I. Kolingerova [2003]. 'An incremental construction algorithm for Delaunay triangulation using nearest- point paradigm.' *Int. J. of Geographical Information science*, **17(2)**, pp. 119 – 138.

[62] Zhang, H. W., H. Wang, B. S. Chen & Z. Q. Xie [2008]. 'Analysis of Cosserat materials with Voronoi cell finite element method and parametric variational principle.' *Computer Methods in Applied Mechanics and Engineering*, **197**(6-8), pp. 741–755.